Transition time of a bouncing drop

Yahua Liu [1,*] Seyed Ali Hosseini [2,*] Cong Liu [1] Milo Feinberg [2]
Benedikt Dorschner [2] Zuankai Wang [3,†] and Ilya Karlin [2,‡]

[1]*State Key Laboratory of High-Performance Precision Manufacturing,*
Dalian University of Technology, Dalian 116024, China

[2]*Department of Mechanical and Process Engineering, ETH Zurich, 8092 Zurich, Switzerland*

[3]*Department of Mechanical Engineering, The Hong Kong Polytechnic University, Hong Kong 999077, China*

Contact time of bouncing drops is one of the most essential parameters to quantify the water repellency of surfaces. Generally, the contact time on superhydrophobic surfaces is known to be Weber number independent. Here, we probe an additional characteristic time, *transition time*, inherent in water drops impacting on superhydrophobic surfaces, marking a switch from a predominantly lateral motion to an axial motion. Systematic experiments and numerical simulations show that the transition time is also Weber number independent and accounts for half the contact time. Additionally, we identify a Weber-independent partition of volume at the maximum spreading state between the rim and the lamella and show that the latter contains 1/4 of the total volume of the drop.

I. INTRODUCTION

The impact of drops on solid surfaces is a subject of interfacial hydrodynamics encountered in various applications, from spray-coating to ink-jet printing to cooling [1–4]. Of special interest is the strong repellence observed on superhydrophobic surfaces (SHSs), of particular importance for self-cleaning and anti-icing [5–10]. The standard viewpoint represents drop bouncing off SHSs as a spread-recoil-rebound process. The contact time scales as the (square root of the) ratio between the mass of the droplet and the surface tension and is independent of the impact kinetic energy or the Weber number $\text{We} = \rho U_0^2 R_0 / \gamma$, where U_0, R_0, ρ, and γ are the impact velocity, the radius, the density, and the surface tension of the drop. An elegant explanation is based on a harmonic mode argument [11,12], in which the drop bouncing is mapped onto an equivalent spring-mass system. Recent studies also show that the contact time of bouncing droplets can be significantly reduced by controlling the surface macrotextures [13–17].

In the present work, we take a closer look at the dynamics of drops impacting SHSs through both experiments and simulations. We confirm previous observations on the Weber independence of contact time and further observe that the characteristic time marking a switch from a predominantly radial to an axial motion of the recoiling drop, termed transition time here, is also independent of the Weber number and constitutes a half of the contact time on a flat SHS. This observation, based on identification both through the Worthington jet and the internal viscous dissipation rate of the drop, agrees very well with recent studies on the time evolution of the normal force exerted by a

---

*These authors contributed equally to this work.

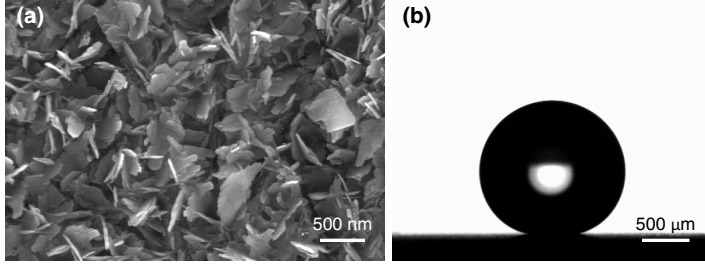†Contact author: zk.wang@polyu.edu.hk

‡Contact author: ikarlin@ethz.ch

FIG. 1. Surface characterization. (a) Scanning electron microscope images of the superhydrophobic surface. (b) Optical image showing an ∼3-μL water drop sitting on the surface.

drop on the substrate [18]. We further analyze the volume distribution at the maximum spreading state and observe the volume partition between the rim and the lamella is also Weber independent.

The paper starts with an overview of both experimental and numerical techniques used in the context of this study. We then present measured transition times and an in-depth analysis of the drop impact process through energy budget and flow field analyses.

II. METHODS

A. Experiments

Drop impact experiments were conducted on a superhydrophobic surface covered by nanosheets fabricated via chemical etching on a copper plate. Specifically, copper blocks with a size of $2 \times 2 \, \text{cm}^2$ were first polished by fine sandpapers (1500#) and then ultrasonically cleaned in ethanol and deionized water for 10 min, respectively, and dried in clean air, followed by immersion in an aqueous solution of 2.5 M/L sodium hydroxide and 0.1 M/L ammonium persulfate for 60 min. To render the surface superhydrophobic, the as-fabricated substrates were then put in 1 mM/L hexane solution of trichloro(1H,1H,2H,2H-perfluorooctyl)silane for ∼60 min, followed by heat treatment at 150 °C in air for 1 h. A scanning electron microscope image of the substrate is shown in Fig. 1. The process resulted in a surface contact angle of $\theta = 166° \pm 3.2°$.

B. Lattice Boltzmann solver for nonideal fluids

The simulations conducted in the present study were performed using the pseudopotential lattice Boltzmann method (LBM) [19]. The discrete populations evolve in time and space and can be expressed as

$$f_i(\boldsymbol{r} + \boldsymbol{c}_i \delta t, t + \delta t) - f_i(\boldsymbol{r}, t) = \frac{\delta t}{\tau} \big[f_i^{\text{eq}}(\rho, \boldsymbol{u}) - f_i(\boldsymbol{r}, t) \big] + f_i^{\text{eq}} \bigg(\rho, \boldsymbol{u} + \frac{\boldsymbol{F} \delta t}{\rho} \bigg) - f_i^{\text{eq}}(\rho, \boldsymbol{u}), \quad (1)$$

where $\boldsymbol{c}_i$ $(i = 1, \dots, Q)$ and δt are the discrete velocities and the discrete time-step size, respectively. We consider the standard $D3Q27$ lattice in three dimensions $(D = 3)$ with 27 velocities $(Q = 27)$, $\boldsymbol{c}_i = (c_{ix}, c_{iy}, c_{iz})$, $c_{i\alpha} \in \{-1, 0, 1\}$. The relaxation time τ is tied to the local dynamic viscosity and density as $\tau = \mu/\rho \varsigma^2 + \delta t/2$ and the discrete equilibrium distribution function, in its full product form, is defined as [20]

$$f_i^{\text{eq}}(\rho, \boldsymbol{u}) = \rho \prod_{\alpha = x, y, z} (1 - \mathcal{P}_{\alpha\alpha})^{1 - |c_{i,\alpha}|} \left(\frac{\mathcal{P}_{\alpha\alpha} + c_{i,\alpha} u_\alpha}{2} \right)^{|c_{i,\alpha}|}, \quad (2)$$

with

$$\mathcal{P}_{\alpha\alpha} = u_\alpha^2 + \varsigma^2, \quad (3)$$

where u is the local fluid velocity and $\varsigma = \delta r / \sqrt{3} \delta t$ is the lattice sound speed. The body force $\boldsymbol{F}$ is defined as [21]

$$\boldsymbol{F} = -\psi(\boldsymbol{r}) \sum_{i=1}^{Q} \frac{w_i}{\varsigma^2 \delta t} \boldsymbol{c}_i [\mathcal{G}_1 \psi(\boldsymbol{r} + \boldsymbol{c}_i \delta t) + \mathcal{G}_2 \psi(\boldsymbol{r} + 2\boldsymbol{c}_i \delta t)], \tag{4}$$

where the potential ψ is computed as

$$\psi = \sqrt{\frac{2(P - \rho \varsigma^2)}{\mathcal{G}_1 + 2\mathcal{G}_2}}. \tag{5}$$

The parameters $\mathcal{G}_1$ and $\mathcal{G}_2$ in Eq. (5) are usually referred to as the interaction strength constants, which in practice are used to keep the term inside the square root positive and set the surface tension, as the latter is tied to $(\mathcal{G}_1 + 8\mathcal{G}_2)/(\mathcal{G}_1 + 2\mathcal{G}_2)$ [21]. In the present work, the Peng-Robinson nonideal equation of state is used for the pressure

$$P = \frac{\rho R T}{1 - b\rho} - \frac{a\alpha(T)\rho^2}{1 + 2b\rho - b^2\rho^2}, \tag{6}$$

where

$$\alpha(T) = 1 + (0.37464 + 1.5422\omega - 0.26992\omega^2)(1 - \sqrt{T/T_c})^2, \tag{7}$$

with $a = 0.45724R^2T_c^2/P_c$ and $b = 0.0778RT_c/P_c$, and T_c and P_c are the critical temperature and pressure, respectively. The acentric parameter ω is set to 0.344. In this research, the nondimensional temperature in the equation of state was set to $T/T_c = 0.74$, resulting in a density ratio of approximately 220.

C. Interface tracking

Here, especially for the second part of the study, we monitor the evolution of different subvolumes within the droplet over time. For that purpose, the LBM solver for the flow field will be supplemented with an interface tracking algorithm. The interface tracking is performed by solving the conservative Allen-Cahn equation,

$$\partial_t \phi + \nabla \cdot \phi \boldsymbol{u} - \nabla \cdot \left[\mathcal{M} \nabla \phi - \boldsymbol{n} \frac{4\phi(1 - \phi)}{\mathcal{W}} \right] = 0, \tag{8}$$

where ϕ is the order parameter, $\mathcal{M}$ is the mobility, $\mathcal{W}$ is the interface thickness, and $\boldsymbol{n}$ is the unit vector normal to the interface defined as

$$\boldsymbol{n} = \frac{\nabla \phi}{||\nabla \phi||}. \tag{9}$$

This system results in a conservative advection of the order-parameter space (representing the diffuse interface) with the fluid velocity field. While this equation can be solved using any of the available different space/time discretization strategies, in the context of the present study a modified advection-diffusion LBM scheme was used. Details of the implementation of this solver can be found in previous research [22]. The interface tracking algorithm is illustrated in Fig. 2.

D. Tracer particles

In addition to interface tracking, tracer particles, distributed within the drop, will also be used to assess the internal dynamics. For the tracer particles, they are considered to be massless point particles. As such, the evolution equation of a given particle i reduces to

$$\frac{d\boldsymbol{r}_i(t)}{dt} = \boldsymbol{v}_i(t), \tag{10}$$
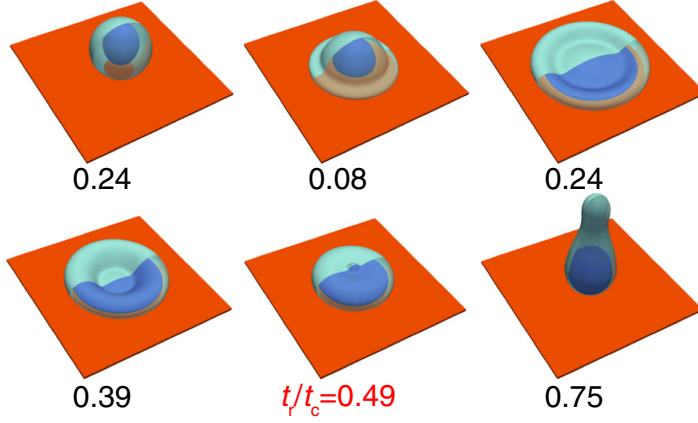
FIG. 2. Evolution of lamella over time as obtained from interface tracking simulations at We $= 18$ and Oh $= 0.035$. Times are normalized by the total contact time t_c. The identification process and meaning of the lamella here are discussed in detail in Sec. IV.

where $\boldsymbol{r}_i$ and $\boldsymbol{v}_i$ are the particle position and velocity, respectively. Given the lack of inertia and volume, it is readily shown that the Maxey-Riley equation for the particle velocity reduces to $\boldsymbol{v}_i(t) = \boldsymbol{u}(\boldsymbol{r}_i, t)$, where the latter is the fluid velocity at the location of the particle at the considered time [23]. The particle space/time evolution equation was solved via integration along the path line and a two-step Runge-Kutta time-marching algorithm. The off-grid fluid velocities needed for the Lagrangian solver were interpolated via third-order Lagrange polynomials from neighboring grid points.

III. WEBER-INDEPENDENT TRANSITION TIME

We consider drop impact on a flat SHS with an apparent contact angle of $166° \pm 3.2°$. Defining the inertia-capillarity time as $\tau_0 = \sqrt{\rho R_0^3 / \gamma}$, we first verified that the contact time scales as $t_c = (2.5 \pm 0.1)\tau_0$ for the Weber number range $1.5 <$ We < 40, consistent with previous observations [11,14]. Below, all times are reported in units of contact time, $\tilde{t} = t/t_c$. Figure 3(a) visualizes a typical drop impact on a SHS at We $= 5.9$, where excellent agreement between experiments and simulations is observed.

The impact process can be decomposed into multiple stages. This includes a first inertia-dominated spreading stage starting immediately after impact and continuing all the way until spreading is slowed down and eventually stopped at maximum spreading due to surface tension. It is interesting to note, and this will be further discussed in later sections, that at this point the drop consists of a flat thin disk we refer to as the lamella, surrounded by a donutlike subvolume we call the rim. This maximum spreading state is then followed by the retraction phase ending with the appearance of the Worthington jet [24], and axial stretching ending with the contact time. Once the drop reaches the maximum spreading at $\tilde{t}_{max} = 0.26$, the retraction starts and is characterized by swelling of the peripheral rim. At $t_r/t_c = 0.47$, the lamella collapses and is entirely absorbed into the receding rim. The collapse of the lamella and subsequent self-collision of the rim at $\tilde{t}_r = 0.47$ leads to the formation of a jetlike structure at the center in the axial direction, also known as the Worthington jet [25,26]. The appearance of this structure, as will be further detailed in the following sections, marks the start of a transfer of momentum/energy from radial to axial. In the context of the present study, we term this instance the *transition* time. Finally, the axially elongated drop leaves the surface at $\tilde{t}_c = 1$.

Transition from the predominantly radial motion to axial motion at $\tilde{t}_r$ highlights two stages in Fig. 3(b), where the lateral extent of the drop was monitored from the initial contact till $\tilde{t}_r$ while the axial elongation was traced thereafter. The drop reaches its maximum radial extent at
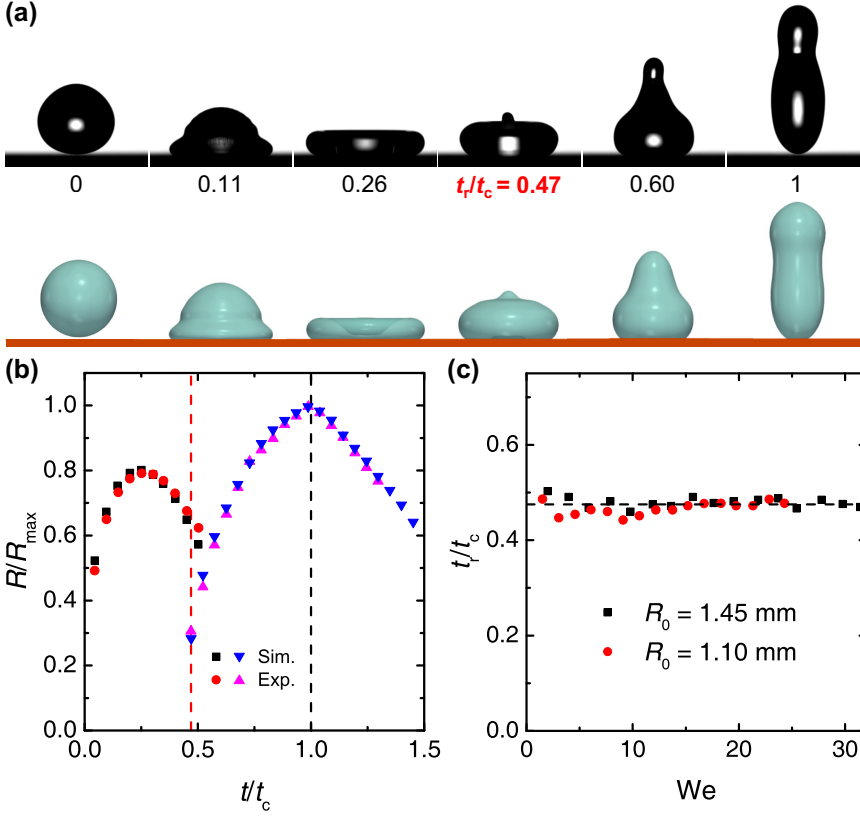
FIG. 3. (a) Snapshots showing different stages of drop impact on a SHS at We = 5.9 from both the experiments and simulations. (b) Evolution of the drop sizes in the radial (red and black) and axial (blue and magenta) directions over time at We = 5.9 from both the experiments and simulations. (c) Normalized transition time $\tilde{t}_r = t_r/t_c$ as a function of We at two drop sizes. The dashed black line is the average transition time from the experiments at $\tilde{t}_r = 0.475$.

$\tilde{t}_{max} = 0.26$, about halfway through the first stage. Once the drop has retracted, the motion switches to predominantly axial, which is represented by a pronounced change in the drop size in the axial direction. Note that the maximum axial elongation is reached halfway through the second stage.

Figure 3(c) shows the transition time $\tilde{t}_r$ over a wide range of Weber numbers with two different drop sizes. The results show that this characteristic time, like the contact time, is Weber independent and also systematically accounts for half of it. It is interesting to note that, though not the focus of the discussion, similar results were also reported in Ref. [18].

For a more quantitative understanding, simulations were run with the LBM [27,28] over $1.5 < $ We < 40 for Oh = 0.2, 0.035, and 0.0063, with Oh $= \sqrt{\text{We}}/\text{Re}$, where the Reynolds number is Re $= R_0 U_0 / \nu$, and ν is the kinematic viscosity of the liquid. Snapshots of drop impact in Fig. 4(a) show excellent qualitative agreement between simulations and experiments. By monitoring the half-maximum height of the drop R_z in Fig. 4(b), the pronounced change of the slope is clearly seen at the experimentally detected transition time.

To better characterize the transition process, we monitor the radial E_r and axial E_a components of kinetic energy and surface energy in Fig. 4(c). At $\tilde{t} = t/t_c = 0.48$, the radial kinetic energy reaches maximum and starts a sharp descent while the axial component E_a follows the opposite trend. This marks the onset of transition which nears completion at $\tilde{t} = 0.53$. Two key observations can be made here: (a) The transition *interval* falls halfway between first and last contact with the
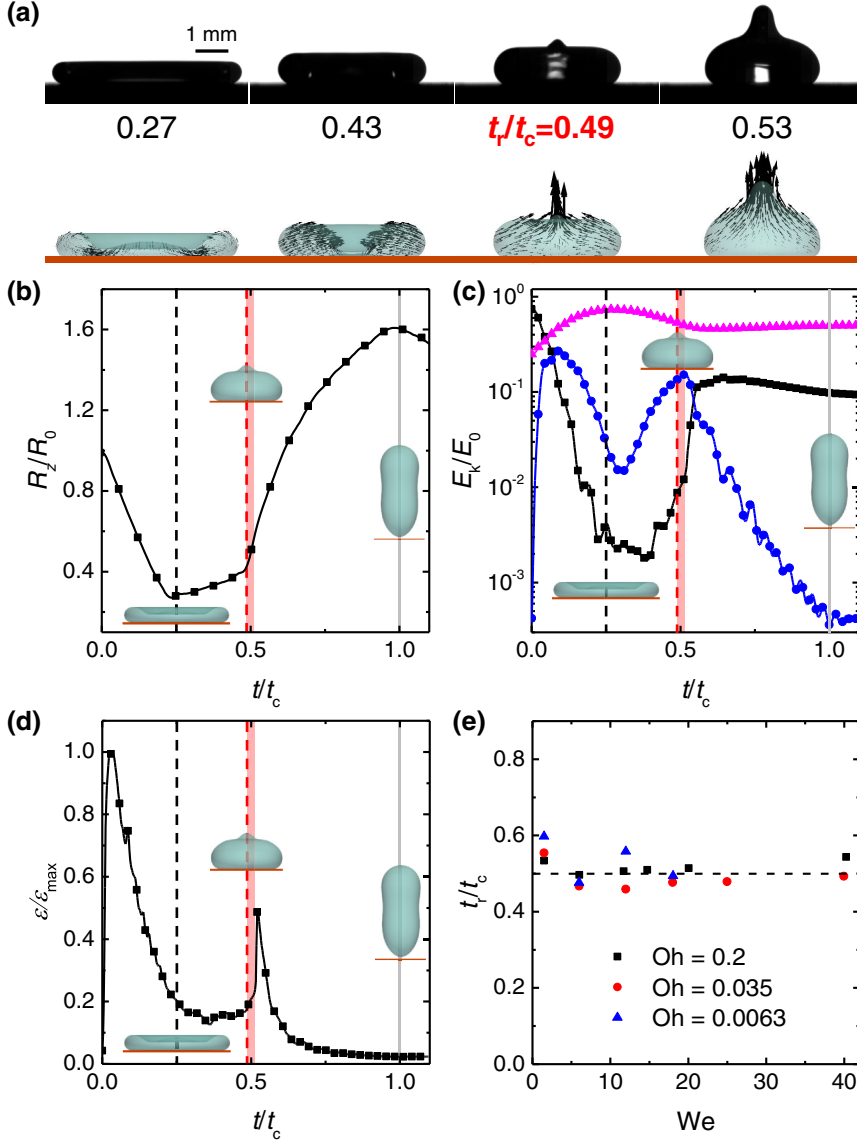
FIG. 4. (a) Selected snapshots from simulation (lower panel) showing the time evolution of a drop bouncing and the arrows indicate the velocity field. The experimental results (upper panel) are presented for comparison. (b) Drop thickness in the axial direction R_z normalized by the initial diameter. (c) Evolution of surface energy (magenta line with triangle markers) and kinetic energy as a function of t/t_c in the radial (blue lines with circular markers) and axial (black line with square markers) directions. (d) Viscous dissipation rate as a function of t/t_c. The black dashed and gray solid lines represent, respectively, the maximum spreading and contact times, while the red dashed line indicates the transition time. The red patch is the transition *interval* obtained from the kinetic energy. Simulation data shown in panels (a), (b), (c), and (d) are at We = 18 and Oh = 0.035. (e) Transition time $\tilde{t}_r$ for different Oh and Oh as obtained from simulations. The dashed black line is the average transition time at $\tilde{t}_r = 0.51$.
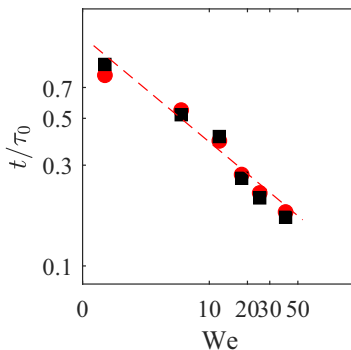
FIG. 5. Time of first dissipation rate peaks from simulations. Red circles are from Oh = 0035 and black squares are from Oh = 0.2. The dashed line represents the $-1/2$ slope.

SHS and (b) is a relatively fast process as compared to spreading and retraction, which can be considered instantaneous on the overall scale of bouncing. Given that transition is characterized by a self-imploding rim leading to considerable velocity gradients, especially at the center of the drop, one would expect the viscous dissipation rate to be affected by the process. The viscous energy dissipation rate [29] can be computed as

$$\epsilon(t) = \frac{\rho \nu}{2} \int_{V_{\text{drop}}} (\nabla \boldsymbol{u} + \nabla \boldsymbol{u}^{\dagger})^2 dV, \tag{11}$$

where $\boldsymbol{u}$ is the local fluid velocity. The dissipation rate, as shown in Fig. 4(d), points to two peaks. The first instance comes up right after the initial impact and corresponds to the dissipation stemming from the impact impulse. A similar first peak in the normal force experienced by the substrate is also reported in Ref. [18]. Based on a simple geometrical argument, one expects to see a peak in the impact force when the largest cross section of the drop has reached the substrate. This in turn means that this *time* would scale with the inertial timescale, i.e., R_0/U_0, which is confirmed in Ref. [18]. Our studies confirm that this time coincides with the first peak in the dissipation rate of the droplet, with a similar scaling, as shown in Fig. 5. The second peak coincides with the appearance of the Worthington jet and the directional transfer of kinetic energy. Transition time based on the dissipation rate at the second peak shown with dashed red lines in Fig. 4(d) agrees well with the visual identification in Fig. 4(e). Thus in the regime of interest, i.e., $1.5 < \text{We} < 40$ and $\text{Oh} < 1$ where the rim forms and maintains integrity throughout impact, the viscous dissipation rate, similar to the second impulse peak detected in Ref. [18] provides an unambiguous measurement of the transition time, that accounts systematically for half of the contact time.

Classically, the independence of the contact time on the Weber number and the scaling $t_c \sim \sqrt{\rho R_0^3/\gamma}$ were explained by viewing the overall bouncing as a single harmonic mode [11,12], with an equivalent spring stiffness γ and mass ρR_0^3. While the spring-mass model can also be used to explain the Weber-independent transition time, as the halfway point of a full oscillation period, in the next section we try to identify characteristic volumes proper to the spreading/retraction phases and discuss another feature observed in our experiments, namely, the Weber independence of the volume partition between two geometrical features of the drop at maximum spreading.

IV. DROP INTERNAL FLOW AND MASS PARTITION

The analysis of Weber-number-independent contact time [11,12] was extended to more complex dynamics to explain reduced contact times on macrostructured SHSs by identifying characteristic subvolumes, termed blobs, governing dynamics of the motion. For instance, in Ref. [14], at maximum spreading, the drop was represented as connected blobs while the estimate for the
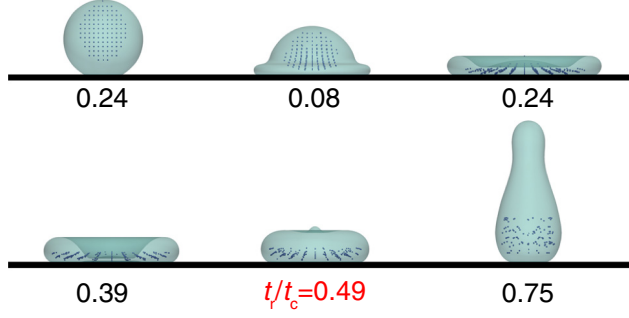
FIG. 6. Evolution of point particles' location over time as obtained from simulations at We $= 18$ and Oh $= 0.035$. Times are normalized by the total contact time t_c.

contact time followed the mass partition among the blobs. Recently, the blob picture explained yet a different scenario, ring-bouncing on a superhydrophobic defect [17]. In all cases, a necessary condition for identification of a characteristic volume/length is its Weber independence. Since the transition time is also Weber independent, a decomposition that follows a mass partition should, in principle, be applicable. For that purpose and to identify characteristic volumes/scales proper to the spreading/retraction phase, we look at the maximum spreading state where two subvolumes, i.e., rim and lamella, can be clearly distinguished. We first explored the evolution of the subvolume resulting in the lamella at maximum spreading over time. In order to visualize its history from the initial impact up to the transition time, the lamella at the maximum spreading was monitored using an interface tracking and massless tracer particles. First, the impacting drop was uniformly seeded with tracer particles monitored forward in time. At maximum spreading, all particles within the lamella were identified and traced *backward* in time to the initial configuration (Fig. 6). An envelope over these particles was used to identify the subvolume V_{lam} which would eventually become the lamella forward in time. In a second run, the subvolume was monitored with both tracer particles and interface tracking, as shown in Fig. 7. Visualization in the figure confirms that the lamella expands and retracts laterally, closely following the radial motion of the drop. The previous geometric argument was supplemented by a study of the flow structure at maximum spreading, e.g., the q-criterion. The q-criterion is defined as the second invariant of the velocity gradient tensor as

$$q = \tfrac{1}{2}[(\mathrm{tr}(\nabla \boldsymbol{u}))^2 - \mathrm{tr}(\nabla \boldsymbol{u} : \nabla \boldsymbol{u})], \tag{12}$$
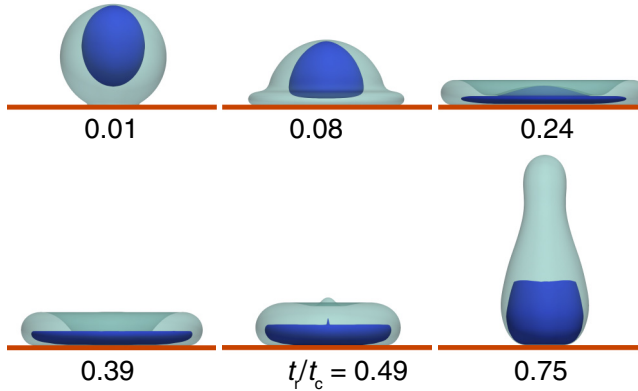

FIG. 7. Evolution of the drop shape and of the lamella (dark blue surface) from simulation at We $= 18$ and Oh $= 0.035$.
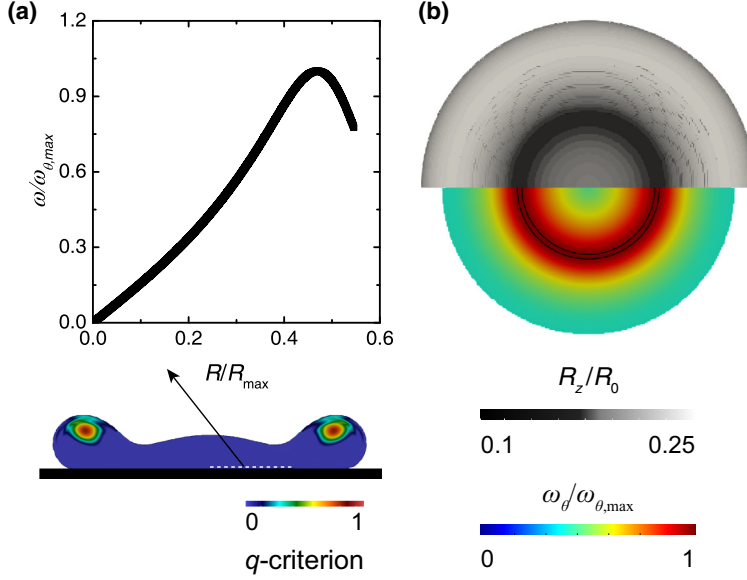
FIG. 8. (a) q-criterion field in a drop at maximum spreading and azimuthal component of vorticity ω_θ normalized by its maximum value $\omega_{\theta,\max}$, in the boundary layer close to the solid substrate. Inset below the drop shows the velocity distribution in the neck region. (b) Top view of the drop at maximum spreading with height distribution (top half) and azimuthal vorticity distribution (bottom half) at the drop interface with the substrate. The maximum vorticity region is shown with black contours. Simulation in panels (a) and (b) is at We = 18 and Oh = 0.035.

where tr indicates the trace of a matrix and ":" is the Frobenius product of two matrices. Positive values of the q-criterion indicate domination of vorticity over the strain rate. The q-criterion field in Fig. 8(a) shows a vortical structure in the rim, in agreement with analogous experiments [30] and simulations [4]. The lamella can be assimilated to an expanding boundary layer [31,32]. Specifically, the initial axial momentum transforms into a radially expanding flow via the no-flux boundary at the substrate surface [31]. Due to viscous effects in the drop and the no-slip boundary condition at the wall, one expects vorticity to be generated in the boundary layer, formed close to the substrate. To verify the existence of this expanding boundary layer, the distribution of the azimuthal component of the vorticity vector, $\omega_\theta = \partial_r u_z - \partial_z u_r$, with u_z and u_r being the axial and radial components of the velocity vector, was computed along the radial axis at the bottom of the lamella, as shown in Fig. 8(b). Farther from the center, the expansion speed increases, leading to larger gradients and therefore larger vorticity up to the neck region, i.e., the onset of the rim, where the flow slows down. A look at the evolution of the volume located in the lamella at maximum spreading and flow structure indicates that the lamella is the characteristic volume associated with the spreading-retraction steps forming the transition time. For the lamella to be the characteristic volume/size, just like the transition time, it must be Weber independent. Based on apparent differences in flow patterns in the lamella and rim through the spreading process, the volume partition between the rim and the lamella was estimated. In experiments, the rim was approximated by a torus based on the top view of the drop at maximum extension (Fig. 9), while in simulations, the interface between was identified via the neck at the outer circumference of the lamella, as shown in Figs. 8(a) and 8(b). Figure 10 shows that the relative volume of the rim constitutes $V_{\mathrm{rim}}/V_0 = 0.75 \pm 0.05$; i.e., the lamella accounts for a quarter of the drop total volume and is Weber independent. This indicates that the prediction by the spring-mass argument holds, $\sqrt{V_{\mathrm{blob}}/V_0} \approx t_r/t_c \approx 1/2$, provided the equivalent volume of the blob associated with the transition
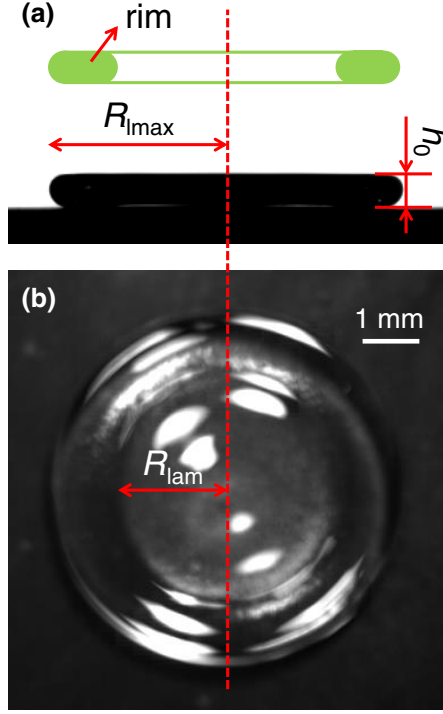
FIG. 9. (a) Side- and (b) top-view images at maximum drop spreading at We = 19.7. Here, R_{lmax}, R_{lam}, and h_0 are the maximum spreading radius, the lamella radius, and the thickness of the rim, respectively.

time is that of the lamella at maximum extension, $V_{blob}/V_0 = V_{lam}/V_0 \approx 1/4$. This observation, i.e., Weber invariance of the volume partition between the rim and the lamella at maximum spreading, along with specific flow dynamics in each subvolume, points to the fact that the lamella can be associated as the characteristic volume to the spreading/retraction phase. This is further confirmed by the fact the relative volume of the lamella at maximum spreading perfectly agrees with previously measured transition times through the spring-mass model.

V. CONCLUSION

In summary, the transition time, visually identifiable via the appearance of the Worthington jet, is shown to be a Weber-independent characteristic time of the drop impact process. This characteristic time was observed to mark the transition of droplet dynamics from radial to axial. The transition time is robust, that is, independent of impact kinetic energy (or Weber number), and accounts systematically for half the contact time. Detailed studies of flow dynamics showed that this instance can be identified through a peak in the dissipation rate within the droplet. A first peak in the dissipation rate, corresponding to a peak in the droplet impact on the substrate, was also identified and shown to be in excellent agreement with observations reported in Ref. [18]. In addition, a detailed study of the flow structure and drop shape at the maximum spreading state showed an additional Weber-independent variable, that is, the volume partition at maximum spreading between the rim and the lamella. Both experiments and simulations confirmed that at maximum spreading the lamella accounts for a quarter of the drop total volume. These observations allowed us to identify the lamella as the blob associated with the spreading/retraction process and explain the fact that the latter systematically accounts for half the contact time through the mass-spring analogy.
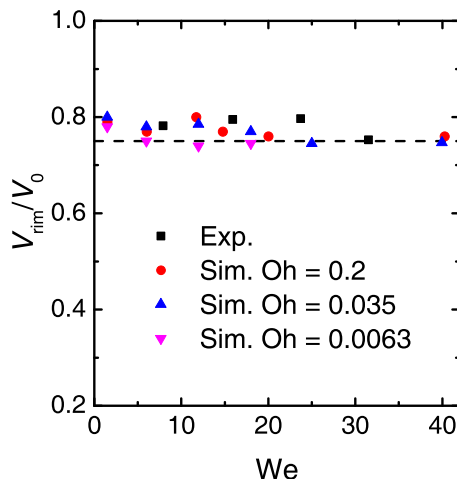
FIG. 10. Volume partition in the drop obtained from both the experiments and the simulations. The dashed black line is the average ratio between the volume of the rim and the drop volume from both numerical and experimental data at $V_{\rm rim}/V_0 = 0.77$.

[1] C. Josserand and S. Thoroddsen, Drop impact on a solid surface, Annu. Rev. Fluid Mech. **48**, 365 (2016).

[2] A. Yarin, Drop impact dynamics: Splashing, spreading, receding, bouncing, Annu. Rev. Fluid Mech. **38**, 159 (2006).

[3] K. Wiedenheft, H. Guo, X. Qu, J. Boreyko, F. Liu, K. Zhang, F. Eid, A. Choudhury, Z. Li, and C. Chen, Hotspot cooling with jumping-drop vapor chambers, Appl. Phys. Lett. **110**, 141601 (2017).

[4] S. Wildeman, C. Visser, C. Sun, and D. Lohse, On the spreading of impacting drops, J. Fluid Mech. **805**, 636 (2016).

[5] J. Lv, Y. Song, L. Jiang, and J. Wang, Bio-inspired strategies for anti-icing, ACS Nano **8**, 3152 (2014).

[6] M. Kreder, J. Alvarenga, P. Kim, and J. Aizenberg, Design of anti-icing surfaces: Smooth, textured or slippery? Nat. Rev. Mater. **1**, 15003 (2016).

[7] H. Stone, Ice-phobic surfaces that are wet, ACS Nano **6**, 6536 (2012).

[8] H. Butt, I. Roisman, M. Brinkmann, P. Papadopoulos, D. Vollmer, and C. Semprebon, Characterization of super liquid-repellent surfaces, Curr. Opin. Colloid Interface Sci. **19**, 343 (2014).

[9] T. L. Liu and C.-J. C. Kim, Turning a surface superrepellent even to completely wetting liquids, Science **346**, 1096 (2014).

[10] D. Wang, Q. Sun, M. Hokkanen, C. Zhang, F.-Y. Lin, Q. Liu, S.-P. Zhu, T. Zhou, Q. Chang, B. He, Q. Zhou, L. Chen, Z. Wang, H. Ras, and X. Deng, Design of robust superhydrophobic surfaces, Nature (London) **582**, 55 (2020).

[11] D. Richard, C. Clanet, and D. Quéré, Contact time of a bouncing drop, Nature (London) **417**, 811 (2002).

[12] K. Okumura, F. Chevy, D. Richard, D. Quéré, and C. Clanet, Water spring: A model for bouncing drops, Europhys. Lett. **62**, 237 (2003).

[13] J. C. Bird, R. Dhiman, H.-M. Kwon, and K. K. Varanasi, Reducing the contact time of a bouncing drop, Nature (London) **503**, 385 (2013).

[14] A. Gauthier, S. Symon, C. Clanet, and D. Quéré, Water impacting on superhydrophobic macrotextures, Nat. Commun. **6**, 8001 (2015).

[15] Z. Wang, C. Lopez, A. Hirsa, and N. Koratkar, Impact dynamics and rebound of water droplets on superhydrophobic carbon nanotube arrays, Appl. Phys. Lett. **91**, 023105 (2007).

[16] Y. Liu, L. Moevius, X. Xu, T. Qian, J. Yeomans, and Z. Wang, Pancake bouncing on superhydrophobic surfaces, Nat. Phys. **10**, 515 (2014).

[17] P. Chantelot, A. Mazloomi Moqaddam, A. Gauthier, S. Chikatamarla, C. Clanet, I. Karlin, and D. Quéré, Water ring-bouncing on repellent singularities, Soft Matter **14**, 2227 (2018).

[18] B. Zhang, V. Sanjay, S. Shi, Y. Zhao, C. Lv, X.-Q. Feng, and D. Lohse, Impact forces of water drops falling on superhydrophobic surfaces, Phys. Rev. Lett. **129**, 104501 (2022).

[19] X. Shan and H. Chen, Lattice Boltzmann model for simulating flows with multiple phases and components, Phys. Rev. E **47**, 1815 (1993).

[20] I. Karlin and P. Asinari, Factorization symmetry in the lattice Boltzmann method, Physica A (Amsterdam, Neth.) **389**, 1530 (2010).

[21] M. Sbragaglia, R. Benzi, L. Biferale, S. Succi, K. Sugiyama, and F. Toschi, Generalized lattice Boltzmann method with multirange pseudopotential, Phys. Rev. E **75**, 026702 (2007).

[22] S. A. Hosseini, H. Safari, and D. Thevenin, Lattice Boltzmann solver for multiphase flows: Application to high Weber and Reynolds numbers, Entropy **23**, 166 (2021).

[23] J. G. M. Kuerten, Point-particle DNS and LES of particle-laden turbulent flow—a state-of-the-art review, Flow, Turbul. Combust. **97**, 689 (2016).

[24] A. M. Worthington, On the forms assumed by drops of liquids falling vertically on a horizontal plate, Proc. R. Soc. Lond. **25**, 261 (1877).

[25] A. M. Worthington and R. S. Cole, V. Impact with a liquid surface, studied by the aid of instantaneous photography, Philos. Trans. R. Soc. Lond. Ser. A **189**, 137 (1897).

[26] A. M. Worthington and R. S. Cole, IV. Impact with a liquid surface studied by the aid of instantaneous photography. Paper II, Philos. Trans. R. Soc. Lond. Ser. A **194**, 175 (1900).

[27] A. Mazloomi M, S. S. Chikatamarla, and I. V. Karlin, Entropic lattice Boltzmann method for multiphase flows, Phys. Rev. Lett. **114**, 174502 (2015).

[28] S. A. Hosseini, B. Dorschner, and I. V. Karlin, Entropic multi-relaxation-time lattice Boltzmann model for large density ratio two-phase flows, Commun. Comput. Phys **33**, 39 (2023).

[29] A. Mazloomi Moqaddam, S. S. Chikatamarla, and I. V. Karlin, Simulation of binary droplet collisions with the entropic lattice Boltzmann method, Phys. Fluids **28**, 022106 (2016).

[30] C. Clanet, C. Béguin, D. Richard, and D. Quéré, Maximal deformation of an impacting drop, J. Fluid Mech. **517**, 199 (2004).

[31] R. D. Schroll, C. Josserand, S. Zaleski, and W. W. Zhang, Impact of a viscous liquid drop, Phys. Rev. Lett. **104**, 034504 (2010).

[32] J. Eggers, M. Fontelos, C. Josserand, and S. Zaleski, Drop dynamics after impact on a solid wall: Theory and simulations, Phys. Fluids **22**, 062101 (2010).